Physics Letters A ••• (••••) ••••••

Contents lists available at ScienceDirect

Physics Letters A

www.elsevier.com/locate/pla

Parametric vibrational resonance in a gyroscope driven by dual-frequency forces

K.S. Oyeleke [a], O.I. Olusola [a,*], U.E. Vincent [b,c], D. Ghosh [d,*], P.V.E. McClintock [c]

[a] Department of Physics, University of Lagos, Lagos, Nigeria
[b] Department of Physical Sciences, Redeemer's University, P.M.B. 230, Ede, Nigeria
[c] Department of Physics, Lancaster University, Lancaster LA1 4YB, United Kingdom
[d] Physics and Applied Mathematics Unit, Indian Statistical Institute, Kolkata 700108, India

ARTICLE INFO

Article history:
Received 28 October 2020
Received in revised form 6 November 2020
Accepted 12 November 2020
Available online xxxx
Communicated by M. Perc

Keywords:
Gyroscope oscillator
Vibrations
Fluctuations
Resonance
Parametric driving

ABSTRACT

We examine and analyze vibrational resonance (VR) in a dual-frequency-driven gyroscope subject to a parametric excitation and an additive periodic forces. The method of direct separation of the fast and slow motions is used to derive the response amplitude analytically from the equation for slow oscillations of the system, in terms of the parameters of the high-frequency signal and the parametric excitation. Numerical simulations are carried out to validate the theoretical results. It is further shown that, when the parametric excitation and additive periodic force consist of low and high frequencies, respectively, a much higher response amplitude can occur. It is about three times larger than the response obtained when the forcing actions are reversed and is attributable to the optimization of low-frequency parametric excitation by the high-frequency additive signal.

1. Introduction

The amplification of a system's response through the actions of two periodic inputs of significantly different frequency – a low frequency (LF) signal and a high frequency (HF) force – now known as vibrational resonance (VR) [1], has become an active field of research during the last two decades. The phenomenon is in many ways similar to stochastic resonance (SR) in which a weak periodic signal in a nonlinear system can be enhanced by additive noise of optimal intensity [2–5], except that in VR the noise is replaced by the HF force.

Work on VR has been motivated in large part by its diverse potential applications in weak signal detection [6,7], output filtering and the attenuation of undesirable signals, as well as the detection of faults in bearings [8–11]. The phenomenon has been explored theoretically [1,6–11,5,12–18] and experimentally [19–21] in bistable and multistable vertical-cavity surface-emitting lasers (VCSELs), and dynamic logic gates in electronic circuits. It has received attention in relation to monostable systems [22], bistable systems [1,23–26], quintic oscillators with and without time-delay [27–29], multistable systems [13,30–32], excitable systems [33,34], scale-free and randomly-connected networks [35,36], neuron models [17,37–40], biological nonlinear maps [41], Morse and Tietz-Hua quantum oscillators for modeling diatomic molecules [42,43], systems with nonlinear damping/dissipation [44–47], fractional order systems [27,48], position-dependent mass oscillator [49] and harmonically trapped potential systems [50]. Very recently, some of us demonstrated response amplification induced by deformation of an asymmetric potential [51] as well as the possibility of roughness-induced resonances in a rough potential [47].

In contrast to the impressive array of theoretical and computational understanding embodied in this large corpus of research on VR, rather less attention has been paid to parametrically-driven nonlinear systems [48,52,53]. Such systems are abundant in nature, however, as well as in a wide range of engineering applications. They can be found in models of Bose-Einstein condensates (BECs) for cold atoms, and in laser models, including semiconductor, diode, and fibre lasers, as well as VCSELs. In diode-lasers for instance, high-frequency modulation constitutes an important building block for the transmitters used for encoding optical communications through cavity loss or pump current modulation [54,55]. In addition, parametric driving plays vital roles in signal amplification, filtering and sensing, in particular in micro- and nanoscale materials [56]. Recently, vibrational resonance has been observed in a model Rayleigh-Plesset bubble oscillator in an incompressible liquid driven by a dual-frequency forcing [57].

* Corresponding authors.
E-mail addresses: iolusola@unilag.edu.ng (O.I. Olusola), dibakar@isical.ac.in (D. Ghosh).

https://doi.org/10.1016/j.physleta.2020.127040

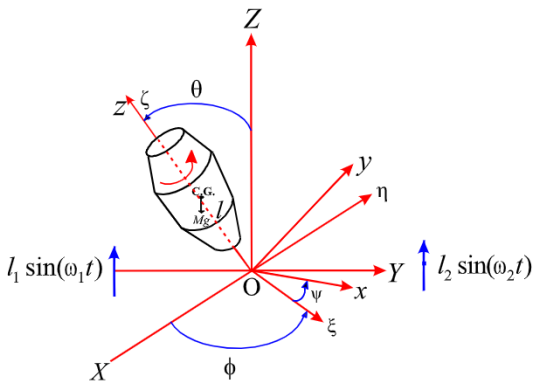

Fig. 1. (Colour online.) Schematic diagram of the dual-frequency-driven gyroscope.

In this paper, we investigate VR in a model of a parametrically-excited gyroscope driven by a periodic force. Research interest in the gyroscope stems largely from its numerous applications in mechanical, optical and micro-electro-mechanical devices where it functions variously as an attitude heading reference system, a gyrocompass, an inertial measurement unit, and in inertial navigational aid systems. We refer readers to Ref. [58] for a recent comprehensive review of a wide range of commercial gyroscope applications and their classifications. Previous works on nonlinear gyroscopes considered bifurcation and chaos in a harmonically excited rate gyro [59] and in a symmetric gyro with linear-plus-cubic damping [60]. Active and backstepping controls were employed to control and synchronize two chaotic nonlinear gyroscopes [61,62]. Other examples include Gaussian, radial, basis-adaptive, backstepping control, which was proposed for modified projective synchronization of unknown heavy symmetric chaotic gyroscope systems [63]. The global synchronization stability criteria of linearly-coupled gyroscopes was examined by Olusola et al. [64].

The aforementioned works on gyroscopes, and many others, considered only single-frequency driving. In this paper, the gyroscope model is driven by dual-frequency forces: a parametric excitation and an additive periodic force. In addition to the well known method of tuning the strength of the high-frequency field in VR, we show that the parametrically excited gyroscope also exhibits VR when the low-frequency parametric excitation is tuned. Furthermore, we demonstrate that a higher response amplitude and a wider response bandwidth are obtained when a low-frequency parametric excitation force cooperates with a high-frequency additive forcing. We discuss the implications of our results for the design of optical measurement devices, where high-frequency response and high bandwidth are desirable.

In section 2, we describe the gyroscope model under study and obtain its potential function for the first time. In section 3 detailed theoretical and numerical analyses are presented for the two scenarios of: (i) a low-frequency parametric excitation with a high frequency additive driving force; and (ii) a high-frequency parametric excitation with a low-frequency additive driving force. The results are summarized and conclusions are drawn in section 4.

2. The model

The system to be considered is a dual-frequency-driven gyroscope model mounted on a vibrating base, as illustrated schematically in Fig. 1. The dynamics can be formulated using the Lagrangian approach associated with the Euler's angles, namely, the nutation (θ), precession (ϕ) and spin (ψ) [60]. The Lagrangian is expressed as:

$$L = \frac{1}{2} I_1(\dot{\theta}^2 + \dot{\phi}^2 \sin^2\theta) + \frac{1}{2} I_3(\dot{\phi}\cos\theta + \dot{\psi})^2 \qquad (1)$$

$$-Mg(l + l_1 \sin(\omega_1 t))\cos\theta - Mgl_2 \sin(\omega_2 t)$$

where I_1 and I_3 are the polar and the equatorial moments of inertia of the gyroscope, respectively. Mg is the gravity force, l_1 is the amplitude of the external excitation disturbance, and ω_1 is the frequency of the external excitation. l_2 is the amplitude of the additive external forcing with frequency ω_2. Coordinates ϕ and ψ are cyclic, and they are absent from the Lagrangian. This provides us with two first integrals of the motion expressing the conjugate momenta as

$$P_\phi = \frac{\partial L}{\partial \dot{\phi}} = I_1 \dot{\phi}\sin^2\theta + I_3(\dot{\phi}\cos\theta + \dot{\psi})\cos\theta, \qquad (2)$$

$$P_\psi = \frac{\partial L}{\partial \dot{\psi}} = I_3(\dot{\phi}\cos\theta + \dot{\psi}) = I_3\omega_z, \qquad (3)$$

where ω_z is the spin velocity of the gyroscope. Using the Routh's procedure and the definitions in Eq. (2), the Routhian of the system becomes

$$R = L - P_\phi\dot{\phi} - P_\psi\dot{\psi}. \qquad (4)$$

Treating it as a single-degree-of-freedom dynamical system, its equation of motion can be obtained from the Euler-Lagrange equation,

$$\frac{d}{dt}\left(\frac{\partial R}{\partial \dot{\theta}}\right) - \frac{\partial R}{\partial \theta} = F_d, \qquad (5)$$

where F_d accounts for all the external contributions, including the dissipative force. The latter is assumed to be of linear-plus-cubic form and is written as,

$$F_d = -D_1\dot{\theta} - D_2\dot{\theta}^3, \qquad (6)$$

where D_1 and D_2 are positive constants. The other components of F_d are the dual frequency driving forces $l_1 \sin\omega_1 t$ and $l_2 \sin\omega_2 t$ as shown in Fig. 1. Accordingly, it is easy to show that the equation governing the gyroscope can be written in dimensionless form as

$$\ddot{\theta} + \alpha^2\left(\frac{(1-\cos\theta)^2}{\sin^3\theta}\right) - B\sin\theta + c_1\dot{\theta} + c_2\dot{\theta}^3 - f_2\sin(\omega_2 t) = 0, \qquad (7)$$

where $B = \beta + f_1\sin(\omega_1 t)$ is a parametric driving force of frequency ω_1, and $f_2\sin(\omega_2 t)$ is an additive driving force of frequency ω_2; $c_1\dot{\theta}$ and $c_2\dot{\theta}^3$ are the linear and cubic nonlinear damping terms, respectively, with coefficients c_1 and c_2. The system (7) has been extensively investigated for $f_2\sin(\omega_2 t) = 0$ and without any attention paid to its potential structure, although the latter is fundamental to its general dynamics. From Eq. (7), we obtain the system's potential in the absence of additive driving as

$$V(\theta) = \frac{\alpha^2}{1+\cos\theta} + (\beta + f_1\sin(\omega_1 t))\cos\theta. \qquad (8)$$

The potential, $V(\theta)$ admits two types of potential structure depending on the values of α and β. For instance, with: $c_1 = 0.5$, $c_2 = 0.05$, $f_1 = f_2 = 0.05$, $\omega_1 = \omega_2 = 2$ and $t = t_n (n = 0, 1, 2, \ldots, \infty)$, $V(\theta)$ takes the forms shown in Fig. 2. Both single and double-well potential shapes can be obtained. Fig. 2(a) shows a single-well potential for $\alpha = 10$ and $\beta = 1$, while Fig. 2(b) shows a double-well potential for $\alpha = 2, \beta = 10$. For the single-well structure, Fig. 2(a), the equilibrium point of the unforced system is located at the origin ($\theta = 0, \dot{\theta} = 0$), around which oscillatory motion occurs along the principal axis of the gyroscope, which coincides with its vertical axis. For the double-well potential, which has a local maximum at $\theta = 0$ (an unstable fixed point) with $\alpha = 2$

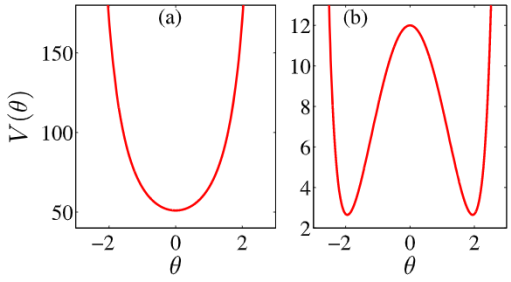

Fig. 2. (Colour online.) The potential of system (7) against θ with the following parameters (a) $\alpha = 10$, $\beta = 1$, $f = 0.05$, $\omega = 2$, $t = t_n$ (single-well), (b) $\alpha = 2$, $\beta = 10$, $f = 0.05$, $\omega = 2$, and $t = t_n$ (double-well).

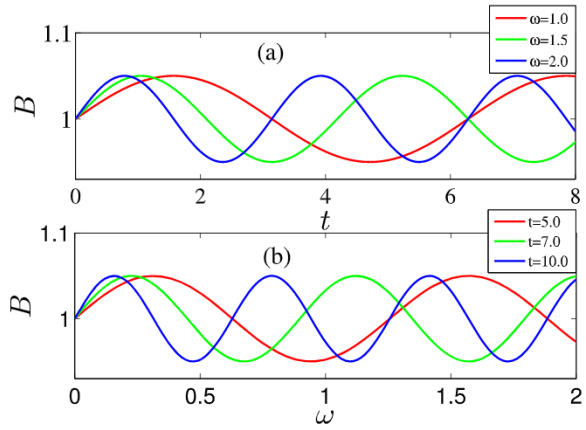

Fig. 3. (Colour online.) Evolution of the parametric driving force, B against t and ω with the following choice of parameters (a) $f = 0.05$, $\beta = 1$, $\omega = [1\ 1.5\ 2]$, (b) $f = 0.05$, $\beta = 1$, $t = [5\ 7\ 10]$.

and $\beta = 10$, there are two local minima located at $\theta = \pm 2$ around which oscillatory motion takes place. The existence of equilibrium is important for the investigation of vibrational resonance [65].

In the absence of the parametric excitation, the shape of the potential, including the positions of the local minima, depends only on the two parameters α and β. This is similar to the case of the Duffing oscillator, in which the shape of the potential also depends on two parameters, ω_0, the natural frequency and β, the parameter controlling the strength of the nonlinearity [14]; but it is unlike the case of quintic oscillators in which the shape of the potential depends on three parameters (ω_o^2, β and γ) [22]. In what follows, we investigate VR in the system (7) under two different conditions: (i) a low-frequency ($\omega_1 = \omega$) parametric excitation force cooperating with a high-frequency ($\omega_2 = \Omega$) additive driving force with $f_1 = f$, $f_2 = G$; and (ii) a high-frequency ($\omega_1 = \Omega$) parametric excitation force cooperating with a low-frequency ($\omega_2 = \omega$) additive driving force, with $f_1 = G$, $f_2 = f$, where $\Omega \gg \omega$ and $G \gg f$.

3. Analysis of vibrational resonance

3.1. CASE ONE: $\omega_1 = \omega$, $\omega_2 = \Omega$, $f_1 = f$ and $f_2 = G$

We first consider the gyroscope model under the action of a weak parametric excitation force of frequency $\omega_1 = \omega$ and a high-frequency additive driving force of frequency $\omega_2 = \Omega$. The potential function is shown in Fig. 2(a). The forms of the parametric driving force B plotted against t and ω are shown in Figs. 3(a) and 3(b), respectively. Note that the period of oscillation decreases with increase in ω and also that, as t increases, the value of ω at which a complete oscillation occurs decreases.

We now analyze VR theoretically in this system, based on the method of direct separation of the slow and fast motions described by Blekhman [12] and further extended by Blekhman and Landa [23]. This is the most effective way of formulating vibrational mechanics problems to obtain the equation of slow motion modulated by the parameters of the fast driving signal. We assume that the solution θ of Eq. (7) consists of a slow motion $X(t)$ with period $2\pi/\omega$ and a fast motion $\psi(t, \Omega t)$ with period $2\pi/\Omega$, i.e.,

$$\theta = X + \psi. \tag{9}$$

In general, the mean value for the fast oscillatory motion is defined as

$$\overline{\psi} = \frac{1}{2\pi}\int_0^{2\pi} \psi dt = 0, \tag{10}$$

and, by substituting Eq. (9) into Eq. (7), one readily obtains,

$$\begin{aligned}\ddot{X} + \ddot{\psi} + \alpha^2 &\left(\frac{(1 - \cos X\cos\psi + \sin X\sin\psi)^2}{(\sin X\cos\psi + sin\psi\cos X)^3}\right)\\ &-[\beta + f\sin(\omega t)](\sin X\cos\psi + \sin\psi\cos X)\\ &+c_1\dot{X} + c_1\dot{\psi} + c_2(\dot{X}^3 + 3\dot{X}^2\dot{\psi} + 3\dot{X}\dot{\psi}^2 + \dot{\psi}^3)\\ &-G\sin(\Omega t) = 0.\end{aligned} \tag{11}$$

Averaging Eq. (11) with respect to the fast motion component yields

$$\begin{aligned}\ddot{X} + \alpha^2 &\left(\frac{(1 - \cos X\overline{\cos\psi} + \sin X\overline{\sin\psi})^2}{(\sin X\overline{\cos\psi} + \overline{\sin\psi}\cos X)^3}\right)\\ &-[\beta + f\sin(\omega t)](\sin X\overline{\cos\psi} + \overline{\sin\psi}\cos X)\\ &+c_1\dot{X} + c_2\dot{X}^3 = 0.\end{aligned} \tag{12}$$

Subtracting Eq. (12) from Eq. (11) yields:

$$\begin{aligned}\ddot{\psi} + \alpha^2 &\left(\frac{(1 - \cos X[\cos\psi - \overline{\cos\psi}] + \sin X[\sin\psi - \overline{\sin\psi}])^2}{(\sin X[\cos\psi - \overline{\cos\psi}] + [\sin\psi - \overline{\sin\psi}]\cos X)^3}\right)\\ &- [\beta + f\sin(\omega t)](\sin X[\cos\psi - \overline{\cos\psi}]\\ &+ [\sin\psi - \overline{\sin\psi}]\cos X) + c_1\dot{\psi} + c_2(3\dot{X}^2\dot{\psi} + 3\dot{X}\dot{\psi}^2 + \dot{\psi}^3)\\ &- G\sin(\Omega t) = 0.\end{aligned} \tag{13}$$

Equations (12) and (13) are the required integro-differential equations of motion for the slow motion X and the fast motion ψ, respectively. Eq. (12) is the more important result from the analysis, being the equation of motion for the slow dynamics, with parametric forcing, which is to be modulated appropriately by varying the parameters of the fast signal. Furthermore, one can impose the inertial approximation $\ddot{\psi} \gg \dot{\psi} \gg \psi$ on Eq. (13) so that $\ddot{\psi} = G\sin(\Omega t)$, which has the solution

$$\psi = -\frac{G}{\Omega^2}\sin\Omega t. \tag{14}$$

With ψ in Eq. (14), and $\overline{\psi}$ given by Eq. (10), we obtain the mean values

$$\overline{\psi} = 0;\ \ \overline{\sin\psi} = \frac{1}{2\pi}\int_0^{2\pi}\sin\psi dt = 0; \tag{15}$$

$$\overline{\cos\psi} = \frac{1}{2\pi}\int_0^{2\pi}\cos\psi dt = J_0\left(\frac{G}{\Omega^2}\right)$$

where $J_0(\frac{G}{\Omega^2})$ is the zeroth-order Bessel function of the first kind.

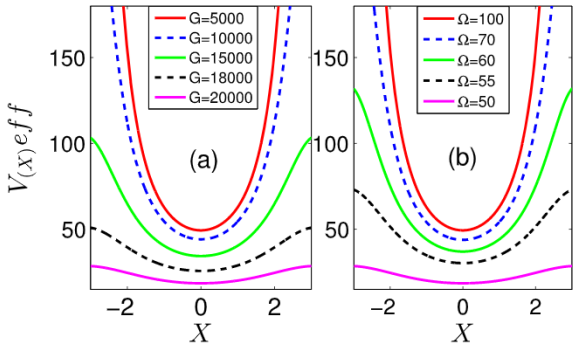

Fig. 4. (Colour online.) The effective potential corresponding to the slow motion of the system the parameters (a) $\alpha = 10$, $\beta = 1$, $\Omega = 100$, $f = 0.05$, $\omega = 2$, $t = t_n$, $G = [5000, 10000, 15000, 18000, 20000]$, (b) $\alpha = 10$, $\beta = 1$, $G = 5000$, $f = 0.05$, $\omega = 2$, $t = t_n$, $\Omega = [100, 70, 60, 55, 50]$.

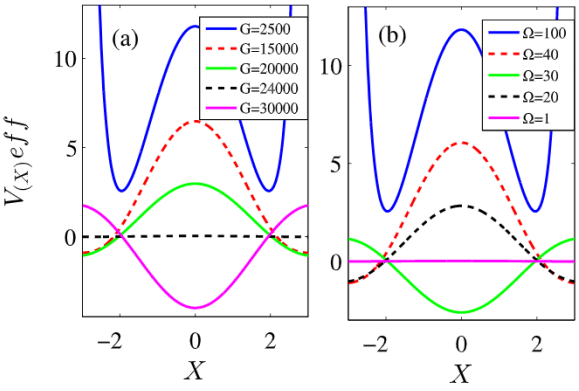

Fig. 5. (Colour online.) The effective potential corresponding to the slow motion of the system for parameters (a) $\alpha = 2$, $\beta = 10$, $\Omega = 100$, $f = 0.05$, $\omega = 2$, $t = t_n$, $G = [2500, 15000, 20000, 24000, 30000]$, (b) $\alpha = 2$, $\beta = 10$, $G = 2500$, $f = 0.05$, $\omega = 2$, $t = t_n$, $\Omega = [100, 40, 30, 20, 1]$.

Substituting solutions (15) into Eq. (12), we have

$$\ddot{X} + \alpha^2 \left(\frac{(1 - J_0(\frac{G}{\Omega^2})\cos X)^2}{(J_0(\frac{G}{\Omega^2})\sin X)^3} \right) \tag{16}$$
$$-[\beta + f\sin(\omega t)]J_0(\frac{G}{\Omega^2})\sin X + c_1\dot{X} + c_2\dot{X}^3 = 0.$$

Equation (16) is the equation of motion for the slow motion of the gyroscope. Its effective potential, V_{eff} is given as:

$$V_{eff}(X) = \frac{\alpha^2 J_0(\frac{G}{\Omega^2})}{(1 + J_0(\frac{G}{\Omega^2})\cos X)}$$
$$+[\beta + f\sin(\omega t)]J_0(\frac{G}{\Omega^2})\cos X. \tag{17}$$

The shape of $V_{eff}(X)$ is dictated by the six parameters α, G, Ω, β, f and ω. Fig. 4 shows plots of V_{eff} against the slow motion component X for selected values of the parameters of the high-frequency signal with fixed values $\alpha = 10$, $\beta = 1$, $f = 0.05$, $\omega = 2$, and at time $t = t_n$. It is clear that, as the parameter G of the fast motion increases, the potential well decreases whereas, as the frequency Ω of the fast motion decreases, the potential well decreases, thereby driving the system into the neutral equilibrium state. Also Fig. 5 shows the plot of V_{eff} against the slow motion component X, for $\alpha = 2$, $\beta = 10$, $f = 0.05$, $\omega = 2$, at time $t = t_n$, such that V_{eff} is a double-well potential. In both Figs. 4 and 5, it can be seen that the shape of the effective potential depends on the parameters of the excitation signal and, in the double-well case shown in Fig. 5, the variation in parameters of the high-frequency signal can energetically initiate potential barrier crossing. Thus the high-frequency force acting as a control input provides the energy requirement for the barrier crossing process.

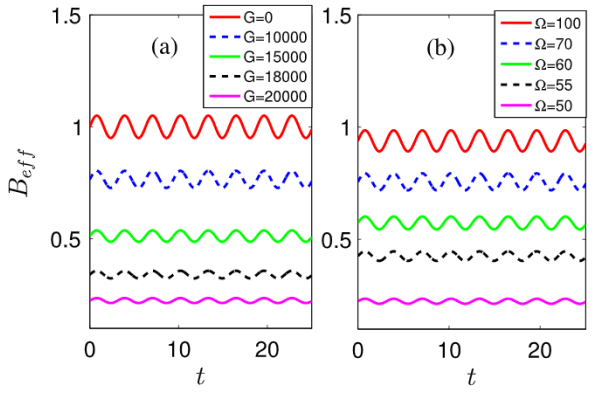

Fig. 6. (Colour online.) Evolution of the effective parametric driving force, B_{eff} against t with the following choice of parameters (a) $\beta = 1$, $\Omega = 100$, $f = 0.05$, $\omega = 2$, $G = [0, 10000, 15000, 18000, 22000]$, (b) $\beta = 1$, $G = 5000$, $f = 0.05$, $\omega = 2$, $\Omega = [100, 70, 60, 55, 50]$.

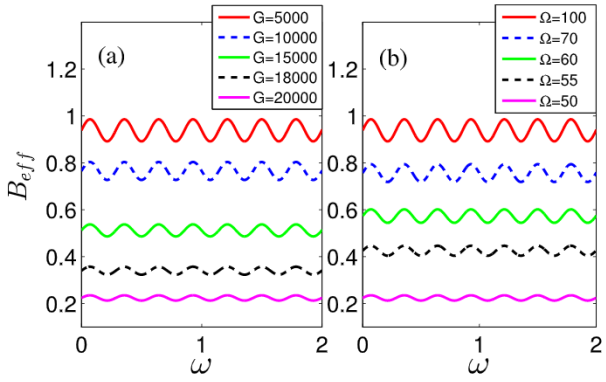

Fig. 7. (Colour online.) Evolution of the effective parametric driving force, B_{eff} against ω with the following choice of parameters (a) $\beta = 1$, $\Omega = 100$, $f = 0.05$, $t = 22$, $G = [0, 10000, 15000, 18000, 22000]$, (b) $\beta = 1$, $G = 5000$, $f = 0.05$, $t = 22$, $\Omega = [100, 70, 60, 55, 50]$.

From Eq. (17), we also deduce that the effective parametric force, B_{eff} is

$$B_{eff} = [\beta + f\sin(\omega t)]J_0\left(\frac{G}{\Omega^2}\right). \tag{18}$$

Equation (18) shows clearly that the effective parametric force is also a function of the parameters of the excitation signal. Plots of B_{eff} against t and ω are shown in Figs. 6 and 7 respectively, where it can be observed that an increase in the parameter G decreases the system's response, whereas an increase in parameter Ω increases the system's response. This again confirms that variations in the parameters of the high frequency forcing impacts on the system's response by excitation of the parameter β.

Considering Eqs. (17) and (18), and Figs. 4–7, it can be seen that the effective potential of the slow motion and the effective parametric driving force depend on the parameters G and Ω of the high-frequency forcing. By varying either G or Ω, the onset of VR can be promoted: either G or Ω can be used to set the equilibrium points of the slow dynamics. This can be computed from Eq. (16) by evaluating $dVeff/dX = 0$, i.e.,

$$\alpha^2 \left(\frac{(1 - J_0(\frac{G}{\Omega^2})\cos X)^2}{(J_0(\frac{G}{\Omega^2})\sin X)^3} \right) -[\beta + f\sin(\omega t)]$$

$$\times J_0\left(\frac{G}{\Omega^2}\right)\sin X = 0, \tag{19}$$

which gives a simple stable equilibrium at $X = X^* = 0$, satisfying stable equilibrium for the single-well potential structure. Note that other stable equilibrium points also exist, satisfying the double-well potential condition.

For simplicity, we assume that the oscillation takes place around the simple equilibrium point X^*. Thus, in what follows, it will be appropriate to treat the oscillation as a deviation from an equilibrium point. Taking the deviation as D, one can write,

$$D = X - X^*, \quad X = D + X^*. \tag{20}$$

Substituting Eq. (20) into Eq. (16) and considering only small deviations, we can approximate $\sin D \approx D$ and $\cos D \approx 1$, so that

$$\begin{aligned}\ddot{D} + c_2\dot{D}^3 + 3c_2\dot{X}^*\dot{D}^2 + (3c_2\dot{X}^{*2} + c_1)\dot{D} \\ +\alpha^2\frac{[(1 - J_0(\frac{G}{\Omega^2})(\cos X^* - D\sin X^*)]^2}{[(J_0(\frac{G}{\Omega^2})(D\cos X^* + \sin X^*)]^3} \\ -P J_0\left(\frac{G}{\Omega^2}\right)(D\cos X^* + \sin X^*) - f\sin(\omega t) = 0,\end{aligned} \tag{21}$$

where

$$P = \beta + f\sin(\omega t) - \frac{f\sin(\omega t)}{J_0(\frac{G}{\Omega^2})(D\cos X^* + \sin X^*)}. \tag{22}$$

If $J_0(\frac{G}{\Omega^2}) > 0$ (< 0), then $X^* = X^*_{min}$ (X^*_{max}). Therefore, $J_0(\frac{G}{\Omega^2})cosX^* = |J_0(\frac{G}{\Omega^2})|$. For $f \gg 1$, we assume that $|D| \gg 1$ so that $\sin D \approx D$. By neglecting the nonlinear terms in Eq. (21), we obtain a linearly-damped driven oscillator whose dynamics may be written as:

$$\ddot{D} + m\dot{D} + \omega_r^2 D = f\sin(\omega t), \tag{23}$$

where $m = 3c_2\dot{X}^{*2} + c_1$ and ω_r is the resonant frequency. At the equilibrium point $X^* = 0, m = c_1$ and $\omega_r^2 = (\beta + f\sin(\omega t))|J_0(\frac{G}{\Omega^2})|$.

Equation (23) has the solution $D(t) = A_L\sin(\omega t + \phi)$ as $t \to \infty$, where ϕ is the phase angle and A_L is given as

$$A_L = \frac{f}{[(\omega_r^2 - \omega^2 + (\alpha^2/(m\omega)))^2 + m^2\omega^2]^{\frac{1}{2}}}. \tag{24}$$

In general, the system's response is defined as

$$Q = \frac{A_L}{f}. \tag{25}$$

Therefore,

$$Q = \left[\left(\omega_r^2 - \omega^2 + \frac{\alpha^2}{m\omega}\right)^2 + m^2\omega^2\right]^{-\frac{1}{2}} \tag{26}$$

and the phase angle ϕ is

$$\phi = \tan^{-1}\left[\frac{m\omega}{\omega^2 - \omega_r^2}\right]. \tag{27}$$

In Eq. (26), setting

$$S = \left(\omega_r^2 - \omega^2 + \frac{\alpha^2}{m\omega}\right)^2 + m^2\omega^2, \tag{28}$$

we have

$$Q = \frac{1}{\sqrt{S}}. \tag{29}$$

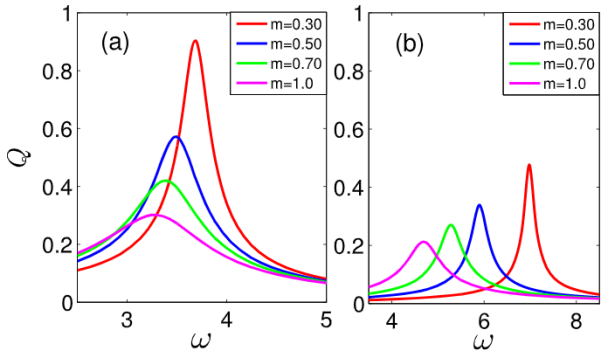

Fig. 8. (Colour online.) Frequency response of the system with different value of m with other parameters fixed at $\Omega = 50$, $f = 0.05$, $t = t_n$, $G = 100$ with (a) double-well case ($\alpha = 2$, $\beta = 10$) and (b) single-well case ($\alpha = 10$, $\beta = 1$).

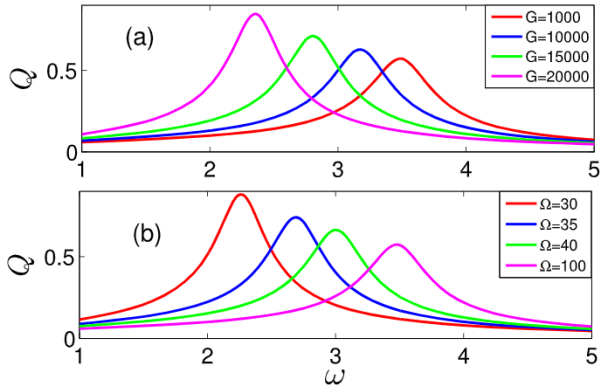

Fig. 9. (Colour online.) Frequency response of the system with different values G and Ω with (a) $c_1 = 0.5$; $c_2 = 0.05$, $\alpha = 2$, $\beta = 10$, $f = 0.05$, $t = t_n$, $\Omega = 100$; (b) $c_1 = 0.5$, $c_2 = 0.05$, $\alpha = 2$, $\beta = 10$, $f = 0.05$, $t = t_n$, $G = 2000$.

Fig. 8 plots the response amplitude, Q versus ω for different values of m, $(m = 3c_2\dot{X}^{*2} + c_1)$ at the equilibrium point $X^* = 0$ for both (a) double-well and (b) single-well potential configurations. This so-called frequency response is widely used in engineering to understand the behaviour of a system under study [65]. Here, the amplitude of the frequency response in the double-well configuration is about twice the amplitude of Q in the single-well case. The figure shows that, as the damping coefficient c_1 or c_2 (or both) increases, Q decreases. There is also a decrease in the value of ω at which the maximum response amplitude occurs. Thus, resonance occurs when Q is a local maximum and this happens whenever S is at a local minimum and is satisfied by $\omega = \omega_r$.

The frequency response for different values of G and Ω is shown in Fig. 9. It is evident that, as predicted theoretically, the value of G or Ω impacts significantly on the frequency response curve. Hence, in practice, one can adjust the parameters of the high frequency forcing (i.e., G and Ω) so as to achieve the desired frequency response, or so as to avoid some undesirable frequencies.

In order to validate the above theoretical analysis, we integrated Eq. (7) numerically using the fourth-order Runge-Kutta algorithm. Equation (7) is expressed as a set of two coupled autonomous ordinary differential equations (ODEs) in the form

$$\frac{d\theta_1}{dt} = \theta_2, \tag{30}$$

$$\begin{aligned}\frac{d\theta_2}{dt} = -\alpha^2(\frac{(1 - cos\theta_1)^2}{\sin^3\theta_1}) + (\beta + f\sin\omega t)\sin\theta_1 \\ -c_1\theta_2 - c_2\theta_2^3 + G\sin(\Omega t).\end{aligned}$$

Equation (30) was integrated with initial conditions $\theta_1(0) = 1$, $\theta_2(0) = 1$, and period, $T = \frac{2\pi}{\Omega}$. The solution corresponds to the first

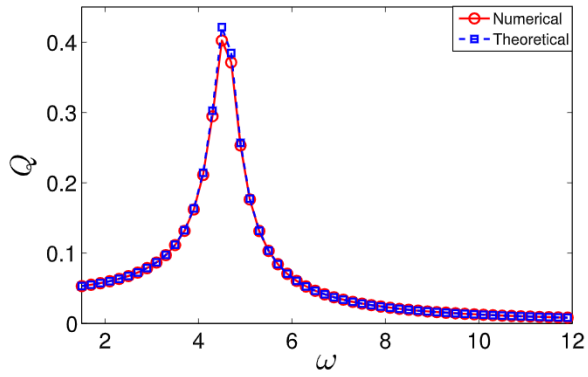

Fig. 10. (Colour online.) Comparison between numerically and theoretically calculated Q plotted against ω with $c_1 = 0.5$, $c_2 = 0.004$, $\alpha = 3$, $\beta = 10$, $f = 0.05$, $\Omega = 50$, $G = 100$.

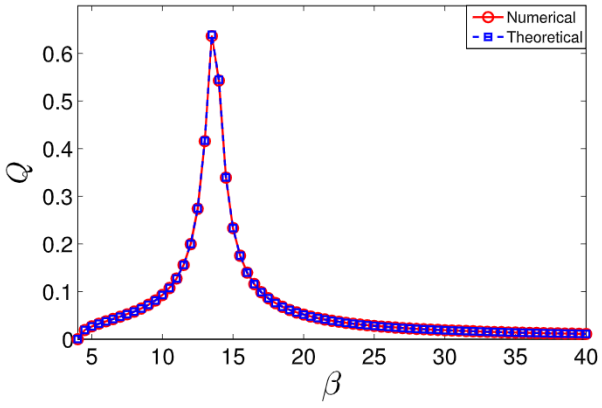

Fig. 11. (Colour online.) Comparison between numerically and theoretically calculated Q plotted against β with $c_1 = 0.3$, $c_2 = 0.001$, $\omega = 5$, $\alpha = 4$, $f = 0.05$, $\Omega = 100$, $G = 100$.

1000 drive cycles of the low-frequency force as a transient. Then, VR was examined by investigating the linear response Q of the low frequency input signal of the gyroscope oscillator, computed numerically using the sine and cosine components of the Fourier series given respectively as

$$Q_s = \frac{2}{nT}\int_0^{nT} \theta(t)\sin\omega t dt, \tag{31}$$

$$Q_c = \frac{2}{nT}\int_0^{nT} \theta(t)\cos\omega t dt,$$

so that,

$$Q = \frac{\sqrt{Q_s^2 + Q_c^2}}{f}. \tag{32}$$

The theoretical Q from Eq. (12) is compared with the numerically computed Q from Eq. (32) as a function of ω in Fig. 10; the simulation parameters were chosen as $c_1 = 0.5$, $c_2 = 0.004$, $\alpha = 3$, $\beta = 10$, $f = 0.05$, $\Omega = 50$ and $G = 100$. The results are in excellent agreement. In both the numerical and theoretical plots, the resonance amplitude of ~ 0.4 is attained at close values of ω. A similar comparison but as a function of parameter β in Fig. 11 also yields excellent agreement; here, the simulation parameters were $c_1 = 0.3$, $c_2 = 0.001$, $\omega = 5$, $\alpha = 4$, $f = 0.05$, $\Omega = 100$, and $G = 100$.

Finally, Fig. 12 shows numerically-computed three-dimensional plots of Q as a function of both ω and β; the simulation parameters were $\alpha = 4$, $G = 100$, $\Omega = 50$, $f = 0.05$, $c_1 = 0.5$, $c_2 = 0.05$, $t = t_n$. The maximum response occurs when $\beta \leq 20$ and $0 < \omega < 5$.

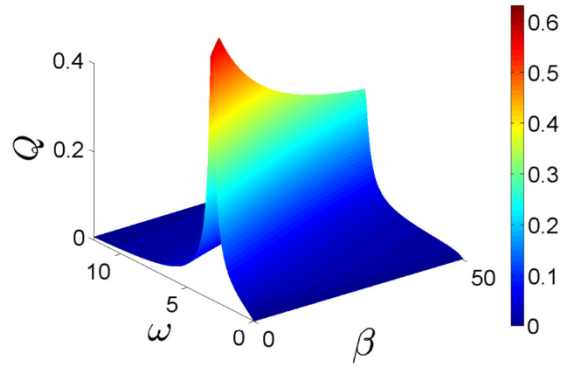

Fig. 12. (Colour online.) 3D plot of Q against ω and β with the following parameters settings $\alpha = 4$, $G = 100$, $\Omega = 50$, $f = 0.05$, $c_1 = 0.5$, $c_2 = 0.05$, $t = t_n$.

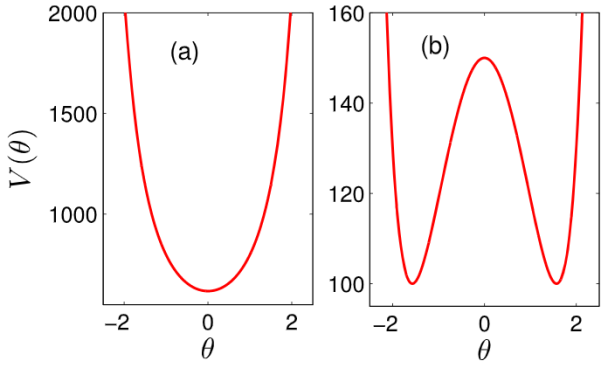

Fig. 13. (Colour online.) The potential $V(\theta)$ of the system (33) given by Eq. (34) against θ for different parameter values. (a) Single-well ($\alpha = 35$, $\beta = 5$, $G = 5000$, $\Omega = 100$, $t = 0$) and (b) Double-well ($\alpha = 10$, $\beta = 100$, $G = 5000$, $\Omega = 100$, $t = 0$.)

3.2. *CASE TWO:* $\omega_1 = \Omega$, $\omega_2 = \omega$, $f_1 = G$, $f_2 = f$

We now consider the case where the gyroscope is parametrically excited by a high frequency periodic force of frequency $\omega_1 = \Omega$ and additively driven by a low frequency force of frequency $\omega_2 = \omega$. The equation of motion to be considered becomes:

$$\ddot{\theta} + \alpha^2\left(\frac{(1-\cos\theta)^2}{\sin^3\theta}\right) - B\sin\theta + c_1\dot{\theta} + c_2\dot{\theta}^3 - f\sin(\omega t) = 0, \tag{33}$$

where $B = \beta + G\sin(\Omega t)$ is a high frequency parametric excitation force and $f\sin(\omega t)$ is the low frequency forcing. All other parameters and variables retain their usual meanings. The potential corresponding to Eq. (33) is:

$$V(\theta) = \frac{\alpha^2}{1+\cos\theta} + [\beta + G\sin(\Omega t)]\cos\theta. \tag{34}$$

The following parameters were chosen: $c_1 = 0.5$, $c_2 = 0.05$, $f = 0.05$ and $\omega = 2$. The potential $V(\theta)$ is plotted against θ for different values of α and β in Fig. 13. Beside the single-well potential structure for $\alpha = 35$, $\beta = 5$ and $t = 0$, the double-well structure when $\alpha = 10$, $\beta = 100$ and $t = 0$ has a potential barrier about ten times higher than the potential structure of *Case One* shown in Fig. 2(b). Its local maximum is located at $\theta = 0$ and its two local minima are located at $\theta = \pm 2$.

By applying the method of separation of fast/slow motions for the analysis of VR, as before, we obtain the equation of motion for the slow dynamics:

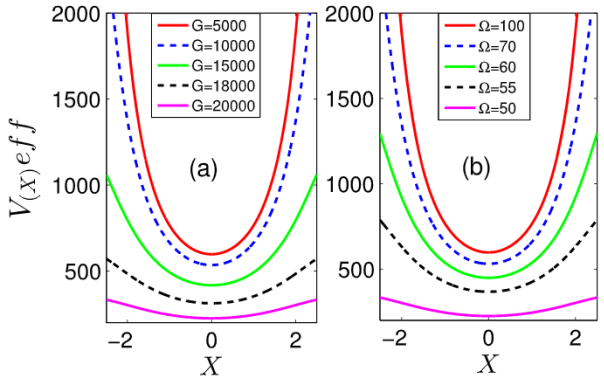

Fig. 14. (Colour online.) The effective potential corresponding to the slow motion of system against X with the following parameters (a) $\alpha = 35$, $\beta = 5$, $\Omega = 100$, (b) $\alpha = 35$, $\beta = 5$, $G = 5000$.

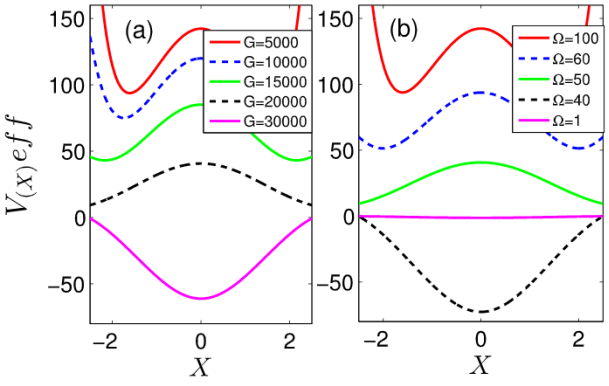

Fig. 15. (Colour online.) The effective potential corresponding to the slow motion of system against X with the following parameters (a) $\alpha = 10$, $\beta = 100$, $\Omega = 100$, (b) $\alpha = 10$, $\beta = 100$, $G = 5000$.

$$\ddot{X} + \alpha^2 \left(\frac{(1 - J_0(\frac{G}{\Omega^2}) \cos X)^2}{(J_0(\frac{G}{\Omega^2}) \sin X)^3} \right) - \beta J_0 \left(\frac{G}{\Omega^2} \right) \sin X + c_1 \dot{X} + c_2 \dot{X}^3 = f \sin(\omega t). \tag{35}$$

Its effective potential $V_{eff}(X)$ is

$$V_{eff}(X) = \frac{\alpha^2 J_0(\frac{G}{\Omega^2})}{(1 + J_0(\frac{G}{\Omega^2}) \cos X)} + \beta J_0 \left(\frac{G}{\Omega^2} \right) \cos X. \tag{36}$$

Comparing Eq. (36) and Eq. (17), we find a significant difference. Eq. (17) is dependent on the parametric excitation force $f \sin(\omega t)$ which contributes to the shape of $V_{eff}(X)$, whereas in Eq. (36) the shape of $V_{eff}(X)$ is independent of the parametric excitation. This difference is nontrivial and clearly has consequences for the system's response.

Fig. 14 plots V_{eff} against the slow-motion component X for selected values of the parameters G and Ω of the high-frequency parametric driving force; the other parameter values were $\alpha = 35$, $\beta = 5$ and $t = 0$. Note that Figs. 13(a) and 14 are similar when the parameters are fixed at $\alpha = 35$, $\beta = 5$, $t = 0$, $\Omega = 100$ and $G = 5000$. Fig. 14(a) shows that the depth of the potential well decreases with increased variation in G, while Fig. 14(b) shows that the depth of the well also decreases with decreased variation in Ω. Again, we plot V_{eff} in Fig. 15 for the double-well potential configuration. We find that Fig. 15 is similar to Fig. 13(b) when the parameters are fixed at $\alpha = 10$, $\beta = 100$, $t = 0$, $\Omega = 100$ and $G = 5000$. In both Figs. 14 and 15 the shape of the effective potential depends largely on the parameters G and Ω of the high frequency

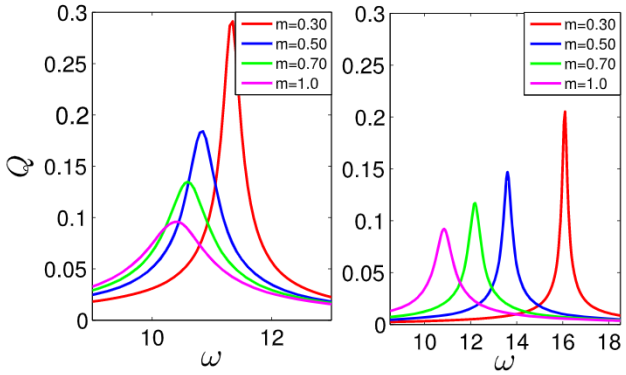

Fig. 16. (Colour online.) Frequency response of the system with (a) double-well case ($\alpha = 10$, $\beta = 100$) and (b) single-well case ($\alpha = 35$, $\beta = 5$).

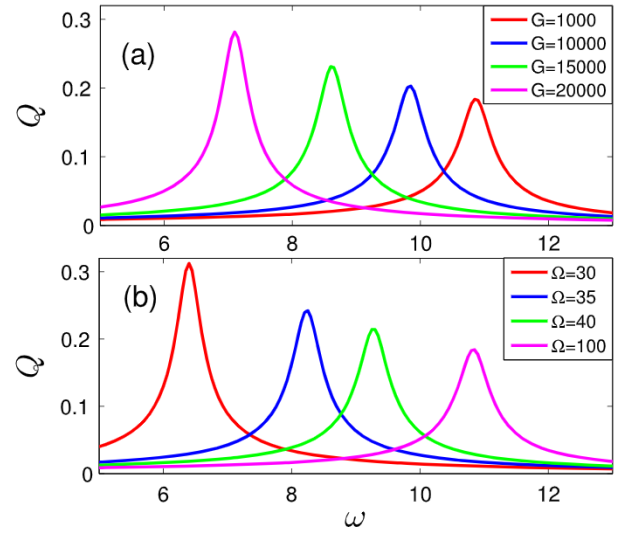

Fig. 17. (Colour online.) Frequency response of the system with different values G and Ω with (a) $c_1 = 0.5$, $c_2 = 0.05$, $\alpha = 10$, $\beta = 100$, $\Omega = 100$, (b) $c_1 = 0.5$, $c_2 = 0.05$, $\alpha = 10$, $\beta = 100$, $G = 2000$.

parametric modulating force: the system responds to variation in the parameters (G or Ω) of the fast signal.

Proceeding as before, it is straightforward to obtain a linearly-damped driven oscillator given by

$$\ddot{D} + m\dot{D} + \omega_r^2 D = f \sin(\omega t), \tag{37}$$

where $m = 3c_2 \dot{X}^{*2} + c_1$ is the nonlinear damping and ω_r is the resonant frequency. At $X^* = 0, m = c_1$, and $\omega_r^2 = \beta |J_0(\frac{G}{\Omega^2})|$. Here, the resonance frequency is independent of the low frequency signal as in *Case One* (See Equation (23)). The response amplitude, Q versus ω for different values of m, at equilibrium point $X^* = 0$ is shown in Fig. 16 for both double-well and single-well configurations. Here, the response amplitudes are relatively the same in magnitude. As the damping coefficients c_1 or c_2 (or both) increase, the resonance amplitude, Q decreases, consequently decreasing the value of ω at which the maximum resonance amplitude occurs.

The corresponding solution of Equation (37) is given as $D(t) = A_L \sin(\omega t + \phi)$, in the limit $t \to \infty$, where A_L is given as

$$A_L = \frac{f}{[(\omega_r^2 - \omega^2 + (\alpha^2/m\omega))^2 + m^2\omega^2]^{\frac{1}{2}}}. \tag{38}$$

Following Eqs (25) to (32), one can determine the response amplitude Q. The frequency response for different values of G and Ω is shown in Fig. 17. The value of G or Ω impacts on the frequency

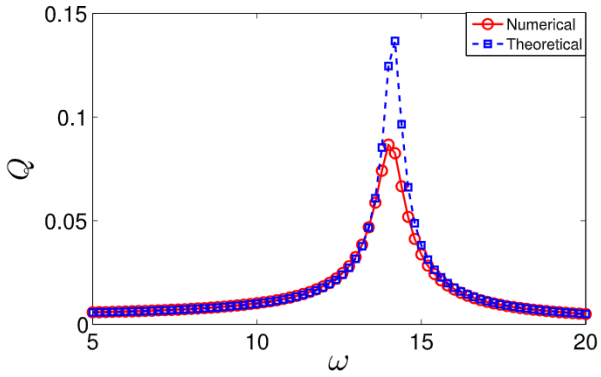

Fig. 18. (Colour online.) Numerically calculated Q versus theoretically calculated Q against ω with $c_1 = 0.5$, $c_2 = 0.05$, $\alpha = 10$, $\beta = 100$, $f = 0.05$, $\Omega = 100$, $G = 200$.

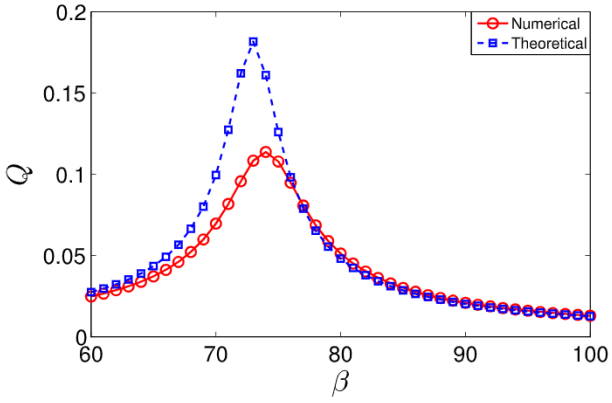

Fig. 19. (Colour online.) Numerically calculated Q versus theoretically calculated Q against β with $c_1 = 0.5$, $c_2 = 0.05$, $\omega = 11$, $\alpha = 10$, $f = 0.05$, $\Omega = 100$, $G = 200$.

response. These parameters (G and Ω) of the high frequency forcing can be adjusted, appropriately, in order to achieve the desired frequency response or to avoid some frequency range.

To validate the theoretical analysis, we integrated Eq. (33) numerically using the same procedure as before with the following fixed parameters: $\alpha = 10$, $\beta = 100$, $\omega = 2$, $c_1 = 0.5$, $c_2 = 0.05$, $f = 0.05$, and the same initial conditions, i.e., $\theta_1(0) = 1, \theta_2(0) = 1$ with period, $T = \frac{2\pi}{\Omega}$. The plots of the theoretical calculated Q and numerically calculated Q against ω, with the following parameters: $f = 0.05$, $\Omega = 100$, $G = 200$ are compared in Fig. 18. The agreement between the numerical and theoretical results is satisfactory given that, in the linear approximation, the average of the parametric forcing $g\sin(\Omega t)$ in Eq. (35) vanishes leaving only the external slow forcing. Fig. 19 shows plots of Q against β for $c_1 = 0.5$, $c_2 = 0.05$, $\omega = 11$, $\alpha = 10$, $f = 0.05$, $\Omega = 100$, $G = 200$. The response amplitudes in both the numerical and the theoretical plots are attained when $\beta \approx 50$. To complete the picture, we show the three-dimensional plot of Q versus ω and β in Fig. 20 with parameters chosen as $\alpha = 10$, $G = 2000$, $\Omega = 100$, $t = 0$, $c_1 = 0.5$ and $c_2 = 0.05$. The low values of the parameter β appear to optimize the low-frequency ω to attain the maximal response.

4. Concluding remarks

In summary, we have investigated the response of a gyroscope oscillator to dual-frequency driving forces in two distinct cases: first, with a weak parametric excitation force of frequency ω and a high-frequency additive force of frequency Ω; and, secondly with a high-frequency parametric excitation force of frequency Ω cooperating with a low-frequency additive force of frequency ω. We considered the response of the oscillator within the framework of vibrational resonance (VR) in which the presence and properties of

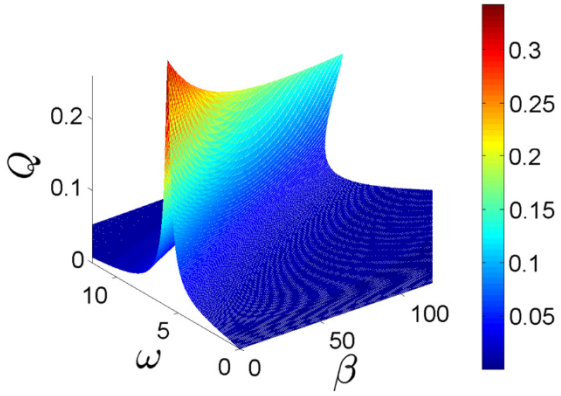

Fig. 20. (Colour online.) 3D plot of Q against ω against β with the following parameters settings $\alpha = 10$, $G = 2000$, $\Omega = 100$, $c_1 = 0.5$, $c_2 = 0.05$.

the high-frequency component can be used to optimize the oscillator's response to the low frequency force. We derived the equation describing the slow motion analytically in terms of the parameters of the two signals, and examined the response outputs for the two cases analyzed. In each case we found that variations in the parameters of the fast signal and the parametric excitation in the equation of the slow motion component lead to the occurrence of VR.

Finally, we highlight some distinctive features of the two simulated cases that constitute the main findings and contributions of this paper, and which could be informative for practical purposes.

(i) The shapes of the effective potential [Eq. (17)] in *Case One*, in which the system is under the action of a weak-frequency parametric excitation are as shown in Figs. 4 and 5. They are determined by the six parameters α, β, f, ω, G and Ω; while in *Case Two*, for which a system parameter is excited by a high-frequency parametric force, the shapes of the effective potential [Eq. (36)] shown in Fig. 14 and 15 are determined by the four parameters α, β, G and ω.

(ii) The resonance frequency ω_r in *Case One* is dependent on the parameters of the parametric excitation, whereas in *Case Two*, it is independent of the parameters of the excitation force.

(iii) The response amplitude in *Case One* is about three times higher than that of *Case Two*. This difference is especially striking when one compares Figs. 8 and 16. Here, the higher amplitude in Fig. 8 arises from the contributory action of the low-frequency excitation, optimized by the high-frequency additive signal which, in effect, is absent when the forcing actions are reversed.

(iv) In *Case One*, the Q versus β plot exhibited a much stronger resonance than Q versus ω (Figs. 10 and 11) whereas in *Case Two*, there is no significant difference between the response curves (cf. Figs. 18 and 19).

(v) A narrower bandwidth was observed in *Case One*, in contrast to the wider modulation bandwidth found in *Case Two* where the system parameter is excited by a high-frequency parametric force.

(vi) In *Case One*, the amplitude of the frequency response in the double-well configuration is about twice, in magnitude, the amplitude of Q in the single-well case whereas in *Case Two*, the amplitudes are similar.

The information provided in (iii) and (iv) may be useful for the design of measurement techniques where a high-frequency response is required [66]. In connection with (v), higher laser modulation bandwidths are desirable qualities for applications in multigigabit

optical fibre transmitters [55]. Thus, high-frequency parametric vibrations could readily be exploited for practical applications.

CRediT authorship contribution statement

K.S. Oyeleke, O.I. Olusola: Conceptualization, Formal analysis, Investigation, Methodology, Validation, Visualization, Writing – original draft; **U.E. Vincent, D. Ghosh, P.V.E. McClintock**: Supervision, Conceptualization, Validation, Visualization, Writing – review & editing.

Declaration of competing interest

The authors declare that they have no known competing financial interests or personal relationships that could have appeared to influence the work reported in this paper.

Acknowledgements

We acknowledge useful discussions with Dr. J.A. Laoye of Department of Physics, Olabisi Onabanjo University Ago-Iwoye, Ogun State, Nigeria and Dr. S.A. Adesanya, Department of Mathematical Sciences, Redeemer's University, Nigeria. We are grateful for support from the Engineering and Physical Sciences Research Council (United Kingdom) under research grants Nos. EP/D000610/1 and EP/M015831/1.

References

[1] P.S. Landa, P.V.E. McClintock, Vibrational resonance, J. Phys. A, Math. Gen. 33 (2000) L433–L438.
[2] R. Benzi, A. Sutera, A. Vulpiani, The mechanism of stochastic resonance, J. Phys. A, Math. Gen. 14 (11) (1981) L453–L457.
[3] M.I. Dykman, D.G. Luchinsky, R. Mannella, P.V.E. McClintock, N.D. Stein, N.G. Stocks, Stochastic resonance in perspective, Nuovo Cimento D 17 (7) (1995) 661–683.
[4] L. Gammaitoni, P. Hänggi, P. Jung, F. Marchesoni, Stochastic resonance, Rev. Mod. Phys. 70 (1998) 223–287.
[5] P. Sarkar, S. Paul, D. Shankar Ray, Controlling subharmonic generation by vibrational and stochastic resonance in a bistable system, J. Stat. Mech. Theory Exp. 2019 (6) (2019) 063211.
[6] H. Liu, X. Liu, J. Yang, M.A.F. Sanjuán, G. Cheng, Detecting the weak high-frequency character signal by vibrational resonance, Nonlinear Dyn. 89 (2017) 2621–2628.
[7] Y. Ren, Y. Pan, F. Duan, F. Chapeau-Blondeau, D. Abbott, Exploiting vibrational resonance in weak-signal detection, Phys. Rev. E 96 (2017) 022141.
[8] Y. Liu, Z. Dai, S. Lu, F. Liu, J. Zhao, J. Shen, Enhanced bearing fault detection using step-varying vibrational resonance based on Duffing oscillator nonlinear system, Shock Vib. 2017 (2017) 5716296.
[9] J.H. Yang, M.A.F. Sanjuán, H.G. Liu, Enhancing the weak signal with arbitrary high-frequency by vibrational resonance in fractional-order Duffing oscillators, J. Comput. Nonlinear Dyn. 12 (5) (2017) 051011.
[10] J.X. Gao, J.H. Yang, D.W. Huang, H.G. Liu, S.Y. Liu, Experimental application of vibrational resonance on bearing fault diagnosis, J. Braz. Soc. Mech. Sci. Eng. 41 (1) (2019) UNSP 6.
[11] L. Xiao, X.-H. Zhang, S. Lu, T.-B. Xia, L.-F. Xi, A novel weak-fault detection technique for rolling element bearing based on vibrational resonance, J. Sound Vib. 438 (2019) 490–505.
[12] I.I. Blekhman, Vibrational Mechanics, World Scientific, Singapore, 2000.
[13] S. Rajasekar, K. Abirami, M.A.F. Sanjuan, Novel vibrational resonance in multistable systems, Chaos 21 (3) (2011) 033106.
[14] S. Jeyakumari, V. Chinnathambi, S. Rajasekar, M.A.F. Sanjuan, Vibrational resonance in an asymmetric Duffing oscillator, Int. J. Bifurc. Chaos 21 (01) (2011) 275–286.
[15] Y. Qin, J. Wang, C. Men, B. Deng, X. Wei, Vibrational resonance in feedforward network, Chaos 21 (2011) 023133.
[16] H. Yu, J. Wang, C. Liu, B. Deng, X. Wei, Vibrational resonance in excitable neuronal systems, Chaos 21 (4) (2011) 043101.
[17] X.-X. Wu, C. Yao, J. Shuai, Enhanced multiple vibrational resonances by Na^+ and K^+ dynamics in a neuron model, Sci. Rep. 5 (2015) 7684.
[18] A. Bashan, A novel approach via mixed Crank-Nicolson scheme and differential quadrature method for numerical solutions of mKdV equation, Pramana J. Phys. 92 (2019) 1–17.
[19] J.P. Baltanás, L. López, I.I. Blechman, P.S. Landa, A. Zaikin, J. Kurths, M.A.F. Sanjuán, Experimental evidence, numerics, and theory of vibrational resonance in bistable systems, Phys. Rev. E 67 (2003) 066119.
[20] V.N. Chizhevsky, E. Smeu, G. Giacomelli, Experimental evidence of vibrational resonance in an optical system, Phys. Rev. Lett. 91 (2003) 220602.
[21] P. Venkatesh, A. Venkatesan, Vibrational resonance and implementation of dynamic logic gate in a piecewise-linear Murali–Lakshmanan–Chua circuit, Commun. Nonlinear Sci. Numer. Simul. 39 (2016) 271–282.
[22] S. Jeyakumari, V. Chinnathambi, S. Rajasekar, M.A.F. Sanjuan, Single and multiple vibrational resonance in a quintic oscillator with monostable potentials, Phys. Rev. E 80 (2009) 046608.
[23] I.I. Blekhman, P.S. Landa, Conjugate resonances and bifurcations in nonlinear systems under biharmonical excitation, Int. J. Non-Linear Mech. 39 (3) (2004) 421–426.
[24] C. Yao, Y. Liu, M. Zhan, Frequency-resonance-enhanced vibrational resonance in bistable systems, Phys. Rev. E 83 (2011) 061122.
[25] V.N. Chizhevsky, Vibrational higher-order resonances in an overdamped bistable system with biharmonic excitation, Phys. Rev. E 90 (2014) 042924.
[26] V.N. Chizhevsky, Analytical study of vibrational resonance in an overdamped bistable oscillator, Int. J. Bifurc. Chaos 18 (06) (2008) 1767–1773.
[27] T.L.M. Djomo Mbong, M.S. Siewe, C. Tchawoua, The effect of the fractional derivative order on vibrational resonance in a special fractional quintic oscillator, Mech. Res. Commun. 78 (2016) 13–19.
[28] Z. Yan, W. Wang, X. Liu, Analysis of a quintic system with fractional damping in the presence of vibrational resonance, Appl. Math. Comput. 321 (2018) 780–793.
[29] W. Guo, L. Ning, Vibrational resonance in a fractional order quintic oscillator system with time delay feedback, Int. J. Bifurc. Chaos 30 (02) (2020) 2050025.
[30] J.H. Yang, X.B. Liu, Controlling vibrational resonance in a multistable system by time delay, Chaos 20 (3) (2010) 033124.
[31] V.N. Chizhevsky, Experimental evidence of vibrational resonance in a multistable system, Phys. Rev. E 89 (2014) 062914.
[32] T. Qin, T. Xie, M. Luo, K. Deng, Vibrational resonance in fractional-order overdamped multistable systems, Chin. J. Phys. 55 (2) (2017) 546–555.
[33] E. Ullner, A. Zaikin, J. García-Ojalvo, R. Báscones, J. Kurths, Vibrational resonance and vibrational propagation in excitable systems, Phys. Lett. A 312 (5) (2003) 348–354.
[34] L. Yang, W. Liu, M. Yi, C. Wang, Q. Zhu, X. Zhan, Y. Jia, Vibrational resonance induced by transition of phase-locking modes in excitable systems, Phys. Rev. E 86 (2012) 016209.
[35] M. Uzuntarla, E. Yılmaz, A. Wagemaker, M. Ozer, Vibrational resonance in a heterogeneous scale free network of neurons, Commun. Nonlinear Sci. 22 (2015) 367–374.
[36] Y. Qin, C. Han, Y. Che, J. Zhao, Vibrational resonance in a randomly connected neural network, Cogn. Neurodyn. 12 (2018) 509–518.
[37] C. Wang, K. Yang, S.-X. Qu, Vibrational resonance in a discrete neuronal model with time delay, Int. J. Mod. Phys. B 28 (2014) 1450103.
[38] B. Deng, J. Wang, X. Wei, H. Yu, H. Li, Theoretical analysis of vibrational resonance in a neuron model near a bifurcation point, Phys. Rev. E 89 (2014) 062916.
[39] V. Baysal, E. Yilmaz, Effects of electromagnetic induction on vibrational resonance in single neurons and neuronal networks, Physica A 537 (2020) 122733.
[40] M. Ge, L. Lu, Y. Xu, R. Mamatimin, Q. Pei, Y. Jia, Vibrational mono-/bi-resonance and wave propagation in FitzHugh-Nagumo neural systems under electromagnetic induction, Chaos Solitons Fractals 133 (2020) 109645.
[41] S. Rajasekar, J. Used, A. Wagemakers, M. Sanjuan, Vibrational resonance in biological nonlinear maps, Commun. Nonlinear Sci. 17 (8) (2012) 3435–3445.
[42] K. Abirami, S. Rajasekar, M.A.F. Sanjuán, Vibrational resonance in the Morse oscillator, Pramana J. Phys. 81 (1) (2013) 127–141.
[43] O.I. Olusola, O.P. Shomotun, U.E. Vincent, P.V.E. McClintock, Quantum vibrational resonance in a dual-frequency driven Tietz-Hua quantum well, Phys. Rev. E 101 (2020) 052216.
[44] T.L.M. Djomo-Mbong, M. Siewe-Siewe, C. Tchawoua, The effect of nonlinear damping on vibrational resonance and chaotic behavior of a beam fixed at its two ends and prestressed, Commun. Nonlinear Sci. 22 (1) (2015) 228–243.
[45] T.O. Roy-Layinde, J.A. Laoye, O.O. Popoola, U.E. Vincent, Analysis of vibrational resonance in bi-harmonically driven plasma, Chaos 26 (2016) 093117.
[46] T.O. Roy-Layinde, J.A. Laoye, O.O. Popoola, U.E. Vincent, P.V.E. McClintock, Vibrational resonance in an inhomogeneous medium with periodic dissipation, Phys. Rev. E 96 (2017) 032209.
[47] J.A. Laoye, T.O. Roy-Layinde, K.A. Omoteso, O.O. Popoola, U.E. Vincent, Vibrational resonance in a higher-order nonlinear damped oscillator with rough potential, Pramana J. Phys. 93 (6) (2019) 102.
[48] J. Yang, M. Sanjuán, H. Liu, Bifurcation and resonance in a fractional Mathieu-Duffing oscillator, Eur. Phys. J. B 88 (2015) 310.
[49] D. Ghosh, B. Roy, Nonlinear dynamics of classical counterpart of the generalized quantum nonlinear oscillator driven by position dependent mass, Ann. Phys. 353 (2015) 222–237.
[50] K. Abirami, S. Rajasekar, M.A.F. Sanjuan, Vibrational resonance in a harmonically trapped potential system, Commun. Nonlinear Sci. Numer. Simul. 47 (2017) 370–378.

[51] U.E. Vincent, T.O. Roy-Layinde, O.O. Popoola, P.O. Adesina, P.V.E. McClintock, Vibrational resonance in an oscillator with an asymmetrical deformable potential, Phys. Rev. E 98 (2018) 062203.
[52] S. Ghosh, D. Shankar Ray, Optical Bloch equations in a bichromatic field; vibrational resonance, Eur. Phys. J. B 88 (2015) 1434–6036.
[53] S. Roy, D. Das, D. Banerjee, Nonlinear response of a parametric bistable oscillator with multiple excitations, Eur. Phys. J. B 93 (1) (2020) 12.
[54] C. Mayol, R. Toral, C.R. Mirasso, S.I. Turovets, L. Pesquera, Theory of main resonances in directly modulated diode lasers, IEEE J. Quantum Electron. 38 (3) (2002) 260–269.
[55] S. Bennett, C.M. Snowden, S. Iezekiel, Nonlinear dynamics in directly modulated multiple-quantum-well laser diodes, IEEE J. Quantum Electron. 33 (11) (1997) 2076–2083.
[56] A.A. Seshia, M. Palaniapan, T.A. Roessig, R.T. Howe, R.W. Gooch, T.R. Schimert, S. Montague, A vacuum packaged surface micromachined resonant accelerometer, J. Microelectromech. Syst. 11 (6) (2002) 784–793.
[57] K. Omoteso, T. Roy-Layinde, J. Laoye, U.E. Vincent, P.V. McClintock, Acoustic vibrational resonance in a Rayleigh-Plesset bubble oscillator, Ultrason. Sonochem. 70 (2021) 105346.
[58] V.M.N. Passaro, A. Cuccovillo, L. Vaiani, M. De Carlo, C.E. Campanella, Gyroscope technology and applications: a review in the industrial perspective, Sensors-Basel 17 (10) (2017) 2284.
[59] Z.M. Ge, H.K. Chen, Bifurcations and chaos in a rate gyro with harmonic excitation, J. Sound Vib. 194 (1996) 107–117.
[60] H.K. Chen, Chaos and chaos synchronization of a symmetric gyro with linear-plus-cubic damping, J. Sound Vib. 255 (2002) 719–740.
[61] Y. Lei, W. Xu, H. Zheng, Synchronization of two chaotic nonlinear gyros using active control, Phys. Lett. A 343 (1) (2005) 153–158.
[62] B.A. Idowu, U.E. Vincent, A. Njah, Control and synchronization of chaos in nonlinear gyros via backstepping design, Int. J. Nonlinear Sci. 5 (2008) 11–19.
[63] F. Farivar, M.A. Shoorehdeli, M.A. Nekoui, M. Teshnehlab, Chaos control and modified projective synchronization of unknown heavy symmetric chaotic gyroscope systems via Gaussian radial basis adaptive backstepping control, Nonlinear Dyn. 67 (2012) 1913–1941.
[64] O.I. Olusola, U.E. Vincent, A.N. Njah, B.A. Idowu, Global stability and synchronization criteria of linearly coupled gyroscope, Nonlinear Dyn. Syst. Theory 13 (3) (2013) 258–269.
[65] S. Rajasekar, M. Sanjuán, Nonlinear Resonances, Springer, Germany, 2016.
[66] R.M. Lin, T.Y. Ng, Applications of higher-order frequency response functions to the detection and damage assessment of general structural systems with breathing cracks, Int. J. Mech. Sci. 148 (2018) 652–666.